Development & Validation of Low-Cost, Highly-Durable, Spinel-Based Materials for SOFC Cathode-Side Contact

A Final Report

for

DOE Award No. DE-FE0031187

Reporting Period Start Date: 10/01/2017

Reporting Period End Date: 09/30/2022

Principal Investigator: Prof. Jiahong Zhu, Department of Mechanical Engineering,
Tennessee Technological University, Cookeville, TN 38505

Date Report was Issued: 1/27/2023

DOE Award Number: DE-FE0031187

Sponsoring Program Office: Office of Fossil Energy

Name of Recipient: Tennessee Technological University

Submitting Organization: Tennessee Technological University
1 William L. Jones Drive
Cookeville, TN 38505-0001

DISCLAIMER:

TABLE OF CONTENTS

1. Executive Summary

A cathode-side contact layer is required to provide and maintain stable electrical conduction paths between the interconnect and cathode in a solid oxide fuel cell (SOFC) stack assembly and thus minimize the ohmic resistance and stack power loss. Current cathode-interconnect contact materials are based on noble metals, electrically-conductive perovskites, their composite materials, etc. These materials are either too expensive or do not possess the overall balanced performance required for the cathode-side contact application. To achieve the DOE SOFC system cost and performance stability goals, a new generation of low-cost, high-performance contact materials needs to be developed.

In this project, spinel-based materials thermally converted from the Fe-Ni and Co-Mn based alloy precursors were developed and validated for the cathode-side contact application. The precursor alloy compositions were optimized via a combination of composition screening in the $(Ni,Fe)_3O_4$ and $(Mn,Co)_3O_4$ spinel system, alloy design using physical metallurgy principles, and cost considerations. The alloy powders with the desired composition and particle size were manufactured via gas atomization. The optimal process parameters for thermal conversion of these alloy precursor layers to a spinel-based layer were identified, i.e., 900℃ x 2h in air, which is close to the initial stack firing condition. The area-specific resistances (ASRs) of the interconnect/contact/cathode test assemblies with the developed contact layer were determined for various durations (up to 5000 h) under simulated cathodic operation conditions. Some of the alloy-derived spinel contacts exhibited the lowest ASR and ASR degradation rate. The in-stack performance of the most promising alloy-derived contact layer is currently being evaluated via stack testing.

To reduce the stack cost, the Co-Mn based alloy powders were utilized as the precursor for synthesis of dense spinel-based interconnect coating. By optimizing both the initial powder size/distribution and the alloy powder composition, a dense $(Mn,Co)_3O_4$-based spinel coating was achieved. Furthermore, co-sintering of the coating/contact dual-layer structure under the initial stack firing condition was realized by utilizing the tailored Co-Mn alloy precursors. Cost analysis of the developed technology indicated a total stack cost reduction of around 10.6% with the implementation of co-sintering of the interconnect coating and the contact layer during initial stack firing. Since low-cost processes such as screen printing is utilized in the precursor application and no reduction heat treatment is needed for the coating formation, the developed technology can be readily implemented at the industrial partner’s manufacturing facilities with no additional capital investment needed.

2. Introduction

In a planar SOFC stack, a number of assemblies are stacked together to increase the output voltage and power. Typical cell/stack material choices for intermediate-temperature SOFCs are yttria-stabilized zirconia (YSZ) or doped ceria as electrolyte, (La,Sr)MnO_3 (i.e. LSM), (La,Sr)FeO_3 (i.e. LSF), or (La,Sr)(Fe,Co)O_3 (i.e. LSFC) as cathode, Ni-YSZ cermet as anode, and Cr_2O_3-forming ferritic alloys (e.g. Crofer 22 APU) as interconnect. At both the cathode- and anode-interconnect interfaces, electrical contact layers are required to apply between the interconnect and electrodes during construction of an SOFC stack to provide and maintain stable electrical conduction path between the interconnect and electrodes in a stack assembly and thus minimize the ohmic resistance and stack power loss [1,2]. Fig. 1 schematically illustrates the cathode-interconnect interface, where the contact layer is in direct contact with the cathode and protective coating on the metallic interconnect. Since the cathode-side contact layer experiences an oxidizing environment, and this layer is in contact with both the ceramic cathode and coated metallic interconnect, it is quite challenging to find a "perfect" solution, which is the goal of this research project.

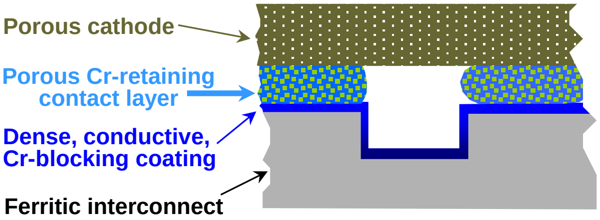

Fig. 1 Schematic drawing of the cathode–interconnect interface in an SOFC stack.

The material requirements for the cathode-side contact are stringent, including: (a) low raw material/processing cost; (b) sufficiently high electrical conductivity (and thus low ASR) over the SOFC lifetime; (c) reasonable match in coefficient of thermal expansion (CTE) with other components; (d) adequate stability/compatibility with adjacent components, especially under a high current of up to 2.0 A/cm^2 encountered during stack operation; (e) appropriate sintering activity and porosity level to provide for additional gas to reach the cathode area; and (f) absence of volatile species such as Cr and Ag for long-term stack performance stability. In addition, it will be highly desirable if the contact material could possess some Cr-retaining capability by (1) acting as a barrier in blocking the Cr transport via solid-state diffusion and/or (2) absorbing Cr species in the contact layer via thermodynamically favorable reactions between the contact material and chromia or Cr vapor species. While a Cr-blocking coating such as $(Mn,Co)_3O_4$ and $CoFe_2O_4$ [3-9] on the interconnects has been demonstrated to effectively reduce the Cr evaporation, a contact layer with additional Cr-retaining capability is likely needed in order to achieve an SOFC stack with longevity (e.g. ~40,000 h for stationary applications).

The state-of-the-art cathode-side contacting approach utilizes an electrically-conductive "contact paste" to fill mechanical gaps in the contact zone and facilitate electrical contact. This paste is normally cured in a dedicated sintering step or during the stack startup firing. The paste can be based on noble metals (e.g. Ag, Pt, and Au), perovskites such as LSM, $(La_{0.8}Sr_{0.2})(Co_{0.5}Fe_{0.5})O_{3-\delta}$ (LSCF) and $(La_{0.8}Sr_{0.2})(Co_{0.5}Mn_{0.5})O_{3-\delta}$ (LSCM), conductive spinels (e.g. Co_3O_4, $(Mn,Co)_3O_4$, $NiCo_2O_4$, and $NiFe_2O_4$), different composites, and other structures [1,2]. The disadvantages for noble metals are their extremely high cost (Au and Pt) and volatility (especially for Ag), while the main concern with perovskites and spinels is the difficulty in balancing their electrical conductivity, CTE, and sinterability. A limited sintering activity at SOFC firing temperatures for conductive oxide contacts will lead to a relatively high ASR and weak adherence to adjacent components, while if a sintering temperature much higher than the SOFC operating temperatures is employed to enhance sintering, excessive interconnect oxidation and detrimental interaction among stack components may lead to high ASRs and poor electrode performance.

A new sintering mechanism, i.e., environmentally-assisted reactive sintering, has been developed to lower the sintering temperature and improve the sinterability of the spinel layer via the utilization of a metallic precursor layer. The enhanced sinterability can be achieved due to the higher amount of heat released during the reaction of metallic powders with oxygen in air to form a spinel phase, high reactivity of the nanoscale oxide phase formed initially on the metal powder surface, and large volume expansion which leads to densification of the contact layer [1]. In this project, both Fe-Ni and Co-Mn based alloy powders will be utilized as the precursor for spinel-base contact synthesis at reduced sintering temperatures. Specific research objectives of this project include: (1) compositional optimization and preparation of the precursor alloy powders; (2) characterization of the specifically-designed alloy-derived contact layer performance in relevant SOFC stack environments, including long-term area-specific resistance (ASR) behavior and in-stack performance of the contact layer in relevant stack operating environments; (3) demonstration /validation of the alloy precursor-derived spinel layer for the cathode-side contacting application; and (4) exploration of potential approaches for further process cost reduction of the spinel-based contact/coating as well as cost analysis to assess the commercial viability of the developed technology.

3. Task 1 – Project Management, Planning and Reporting

Tennessee Technological University (TTU) managed and directed the project in accordance with a Project Management Plan (PMP) to meet all technical, schedule and budget objectives and requirements. The project plans, results, and decisions were appropriately documented and project reporting and briefing requirements were satisfied. The PMP was modified/updated as necessary to accurately reflect current status of the project.

As listed in Table 1, a total of ten milestones were proposed and nine of them were completed as scheduled. The remaining one was not completed on time, due to the test scheduling issues at the industrial collaborator's site. However, the collaborator has promised to share the testing results with TTU once the testing is completed.

Table 1 Milestones of the project

Milestone Title/Description	Planned Start Date	Planned Completion Date	Actual Completion Date	Verification Method	Comments (progress toward achieving milestones, etc.)
Revised Project Management Plan	10/10/2017	10/30/2017	10/23/2017	PMP file	Completed as scheduled
Kickoff Meeting	10/30/2017	12/29/2017	11/29/2017	Presentation file	Completed as scheduled
Compositional optimization of multi-component Fe-Ni-Co based alloy	11/01/2017	06/30/2018	06/28/2018	The optimal Fe/Ni/Co contents as well as other alloy additions are identified.	Completed as scheduled
Atomization of the powder of the optimized alloy	11/15/2017	09/31/2018	09/20/2018	Atomization and analysis of one alloy powder is completed.	Completed as scheduled
Demonstration of long-term ASR stability of the cell with the new contact	01/01/2018	06/30/2019	02/20/2019	The ASR stability over 5,000-h isothermal exposure is demonstrated.	Completed as scheduled
Demonstration of stack performance stability with 1-cell stack testing	04/02/2018	09/30/2019	09/27/2019	Stack performance stability testing for 1,000 h is completed at industrial site.	Completed as scheduled
Synthesis of dense coating on full-size current collector plate	10/20/2019	02/29/2020	12/25/2019	Dense coating on full-size current collector plate is achieved with the metallic precursors.	Completed as scheduled
Stack performance stability evaluation with co-sintered coating/ contact structure	01/20/2021	09/30/22	In progress	Stack durability testing is completed under combined isothermal and cyclic conditions	The assembled stack sent to the industrial partner on 6/23/2022
Cost analysis and commercialization feasibility	01/30/2021	12/31/21	12/31/21	Cost analysis and scale-up feasibility assessment are completed.	Completed as scheduled

4. Task 2 – Optimization of Precursor Alloy Composition

This objective is to optimize the spinel contact composition by clarifying the effects of off-stoichiometry as well further alloying additions on the electrical conductivity and CTEs of spinels in the $(Ni,Fe)_3O_4$ and $(Mn,Co)_3O_4$ systems. Based on the experimental results, the precursor alloy compositions were optimized, which would result in the targeted spinel contact compositions after thermal conversion. The alloy powders with the desired compositions and particle sizes were then manufactured using gas atomization. Also, thermal conversion parameters were identified to achieve an alloy-derived spinel-based contact layer under the SOFC stack firing condition.

4.1 Experimental Methods and Approaches

The $Ni_xFe_{3-x}O_4$ and $Mn_xCo_{3-x}O_4$ powders were prepared via the conventional solid state reaction with high-purity NiO, Fe_2O_3, MnO_2, and Co_3O_4 as the starting materials [10]. After the proper amount of each oxide was weighed according to the desired composition, the precursor oxides were mixed thoroughly, uniaxially compacted at 200 MPa, and then calcined at 900°C for 4 h in air. In addition, various metal oxides as desired were added to the mixture for forming the doped spinels. The pellet was pulverized and sieved. The sieved powder was then mixed with isopropyl alcohol and ball milled for 30 min. The resulting slurry was dried on a hotplate at 95°C and then mixed with 0.5 wt.% polyvinyl butyral (PVB) dissolved in acetone. The powder was compacted uniaxially at 200 MPa into bars with dimensions of roughly 36 × 7 × 3.5 mm and the bars were sintered at different temperatures for different compositions (e.g., 1500°C for 6 h in air for $Ni_xFe_{3-x}O_4$ samples and between 1050 and 1250°C for 6 h for $Mn_xCo_{3-x}O_4$ samples). Efforts were made to make sure the minimization of possible second-phase formation after sintering.

The microstructure of and phases present in the prepared samples were determined by scanning electron microscopy (SEM) and X-ray diffraction (XRD), respectively. The samples were then cut to a length of 25 mm using a double-bladed slow-speed diamond saw. For electrical conductivity measurement, Pt leads were attached to the sample via a Pt paste which was then metallized at 1000 and 900°C for 4 h for $Ni_xFe_{3-x}O_4$ and $Mn_xCo_{3-x}O_4$, respectively. A standard DC 4-probe setup was utilized to measure the electrical conductivity. CTE measurements of the samples were conducted using a push-rod dilatometer (Anter Workhorse II) over the temperature range of 20-800°C in air with a heating rate of 2°C/min.

Based on the electrical conductivity and CTE data of the spinels, optimal spinel compositions were identified for both interconnect coating and cathode-side contact applications. Furthermore, the alloy precursor compositions that could lead to the formation of these spinels upon thermal conversion were identified. The desired precursor alloy powders were then prepared via Ar gas atomization using a Versa-Melt gas atomizer. Several runs of atomization were conducted to achieve the alloy powder purity/size/size distribution suitable for thermal conversion. Moreover, the thermal conversion conditions were varied and the optimal conversion parameters were identified. The conversed spinel layer was characterization by SEM and XRD.

4.2 Results and Discussion

The electrical conductivities of single-phase $Ni_xFe_{3-x}O_4$ and $Mn_xCo_{3-x}O_4$ systems at 800°C can be seen in **Error! Reference source not found.**. As Ni and Mn increase in these spinels, the electrical conductivity decreased. For $Ni_xFe_{3-x}O_4$, the most Fe-rich composition, $Ni_{0.85}Fe_{2.15}O_4$, was found to have the highest conductivity among all the surveyed Ni-Fe spinel compositions, with a conductivity of 14.5 $S{\cdot}cm^{-1}$ at 800°C, while the most Ni-rich composition, $Ni_{1.05}Fe_{1.95}O_4$, had the lowest conductivity (8.16 $S{\cdot}cm^{-1}$ at 800°C). For $Mn_xCo_{3-x}O_4$, the highest electrical conductivity was ~158 $S{\cdot}cm^{-1}$ for $MnCo_2O_4$, the lowest value was ~22 $S{\cdot}cm^{-1}$ for Mn_2CoO_4.

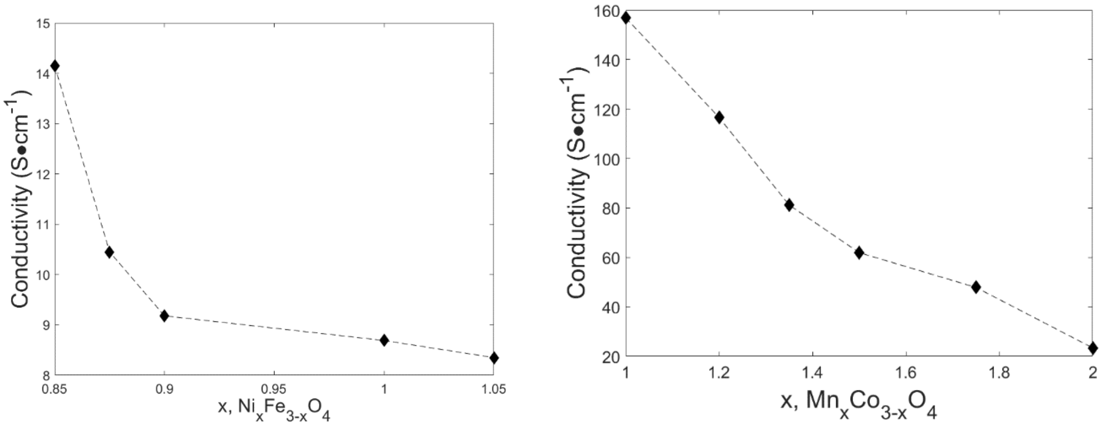

(a) (b)

Fig. 2 Electrical conductivity at 800°C as a function of stoichiometry in $Ni_xFe_{3-x}O_4$ (a) and $Mn_xCo_{3-x}O_4$.

Additional transition-metal addition to the binary spinels could further improve their electrical conductivities. Several doping elements were identified for improving the electrical conductivity of the Fe-rich $NiFe_2O_4$ spinel. As shown in Table 2, the spinels with Ti, Mn, and Co additions exhibited noticeably higher electrical conductivities (as compared to the binary spinel), even though these dopants did not affect the CTE significantly. Even though $Ni_xFe_{3-x}O_4$ exhibited low conductivities, they can be a promising low-cost alternative to the $(Mn,Co)_3O_4$ system for SOFC contact application, if a spinel composition rich in Fe and doped with the promising transition metals is utilized.

Table 2 Electrical conductivities and CTEs of doped $NiFe_2O_4$

Composition	Conductivity at 800°C (S/cm)	Avg. CTE (20-800°C) (ppm/°K)
$Ni_{.84}Fe_{2.16}O_4$	14.4	12.08
$Ni_{.81}Ti_{.03}Fe_{2.16}O_4$	20.49	12.26
$Ni_{.79}Ti_{.05}Fe_{2.16}O_4$	24.43	12.36
$Ni_{.66}Mn_{.03}Co_{.15}Fe_{2.16}O_4$	16.92	11.55
$Ni_{.64}Mn_{.03}Ti_{.02}Co_{.15}Fe_{2.16}O_4$	15.96	12.11

Table 3 lists the average CTEs from room temperature to 800°C for both $Ni_xFe_{3-x}O_4$ and $Mn_xCo_{3-x}O_4$ spinels, as well as the commercial interconnect alloy Crofer 22 APU. Overall, the CTEs of the $Ni_xFe_{3-x}O_4$ spinels were close to 12×10^{-6} K^{-1} and the effect of off-stoichiometry on the CTE was minimal, even though the two most Fe-rich compositions had slightly higher CTEs. All surveyed Ni-Fe spinel compositions were considered to be well-matched in CTE with other SOFC stack components (e.g., 11.80×10^{-6} K^{-1} for Crofer 22 APU) [11-13]. Conversely, the CTE of $Mn_xCo_{3-x}O_4$ spinels was found to be highly sensitive to changes in stoichiometry, decreasing with increasing Mn content. The most Co-rich composition surveyed, $MnCo_2O_4$, exhibited a CTE of 13.35×10^{-6} K^{-1}, while the most Mn-rich one, Mn_2CoO_4, had a CTE of 7.39×10^{-6} K^{-1}.

Table 3 Measured average CTE of spinels in the Ni-Fe and Mn-Co systems from 20-800°C

Composition	**CTE ($\times 10^{-6}$ K^{-1})**
$Ni_{0.85}Fe_{2.15}O_4$	12.10
$Ni_{0.875}Fe_{2.125}O_4$	12.21
$Ni_{0.9}Fe_{2.1}O_4$	11.64
$NiFe_2O_4$	11.74
$Ni_{1.05}Fe_{1.95}O_4$	11.75
$MnCo_2O_4$	13.35
$Mn_{1.2}Co_{1.8}O_4$	12.49
$Mn_{1.35}Co_{1.65}O_4$	11.09
$Mn_{1.5}Co_{1.5}O_4$	10.45
$Mn_{1.75}Co_{1.25}O_4$	8.62
Mn_2CoO_4	7.39
Crofer APU 22	11.80

Considering that Ni-Fe based spinel compositions all appear to be extremely well-matched in CTE for stacks utilizing ferritic alloy interconnects, the optimal composition in the $Ni_xFe_{3-x}O_4$ system would be the most Fe-rich spinel located near the spinel/ (spinel+Fe_2O_3) boundary, which would conceivably exhibit the highest conductivity.

Selection of an optimal composition in the Mn-Co spinel system is more complicated; as both conductivity and CTE increase drastically with the Co content, the composition which has the highest conductivity also exhibits a highly mismatched CTE with other stack components. Based on the results from this study, the intermediate compositions of $Mn_{1.2}Co_{1.8}O_4$ and $Mn_{1.35}Co_{1.65}O_4$ between $Mn_{1.5}Co_{1.5}O_4$ and $MnCo_2O_4$ exhibit better CTE matching and higher conductivities at 800°C (116 and 81.2 $S\cdot cm^{-1}$, respectively). Of these two compositions, $Mn_{1.2}Co_{1.8}O_4$ also avoids the tetragonal ↔ cubic spinel transition upon heating/cooling [10,14,15] and is therefore the more thermally stable composition. Based on these considerations, $Mn_{1.2}Co_{1.8}O_4$ is the optimal composition in the Mn-Co spinel system for the cathode-side contact application.

A number of Fe-Ni and Co-Mn based alloy precursor compositions that would lead to the formation of the promising spinels were selected for powder preparation. For example, Table 4 shows several Co-Mn based alloys and corresponding spinel compositions after thermal conversion. The alloy ingots with the targeted compositions were prepared by arc melting and drop casting. Ar gas atomization was then utilized to atomize the molten material for achieving spherical alloy powders [16]. Several gas atomization parameters such as Ag gas pressure, alloy melt temperature, and liquid metal feeding rate were varied and the optimal atomization parameters were identified and employed for processing the alloy powders.

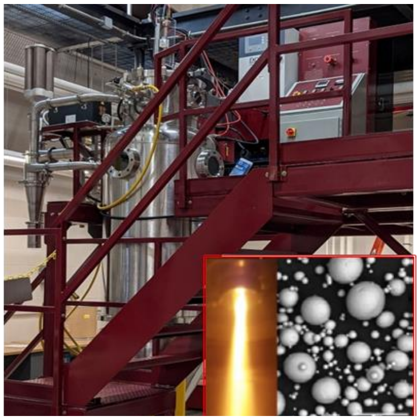

Fig. 3 A picture of the gas atomizer.

Table 4 Chemical compositions of three Co-Mn based alloy powders (wt.%) and the corresponding spinel compositions after thermal conversion

Alloy ID	Co	Mn	Fe	Ce	Spinel Composition
Co-Mn	68.21	31.79	—	—	$MnCo_2O_4$
Co-Mn-Fe	64.72	31.80	3.23	—	$MnCo_{1.9}Fe_{0.1}O_4$
Co-Mn-Fe-Ce	64.72	31.77	3.23	0.41	$MnCo_{1.895}Fe_{0.1}Ce_{0.005}O_4$

Fig. 3 is a picture of the atomizer with the insert showing the atomized metal stream and the resulting powder. Obviously, the alloy powder was highly spherical. A paste containing the alloy powder and some organic binder/liquid was screen printed onto a ferritic alloy substrate. Various sintering temperatures (from 600 to 1000℃) and durations (from 0.5 to 10 h) were utilized to thermally convert the screen-printed alloy precursor layer to the desired spinel layer. One of the best sintering conditions was 900℃ x 2h in air, which is identical to typical stack initial firing condition. As shown in Fig. 4, after 900℃ x 2h sintering a single-phase spinel structure was achieved in the precursor layers with the three alloys listed in Table 4 as well as with the mixed Co and MnO_2 powders. Fig. 5 shows the cross-sectional view of the converted layer with the Co-Mn alloy precursor with a uniform spinel layer achieved.

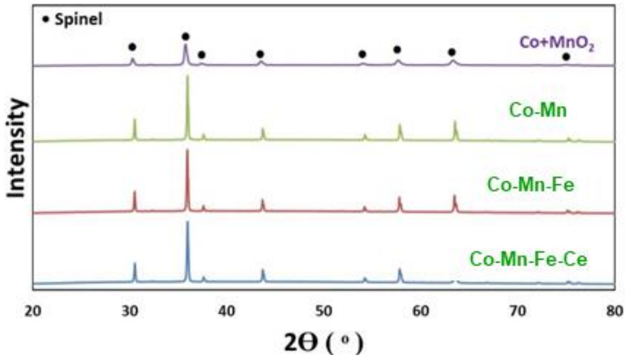

Fig. 4 XRD patterns of the converted layers with different metallic precursors after 900℃ x 2-h sintering.

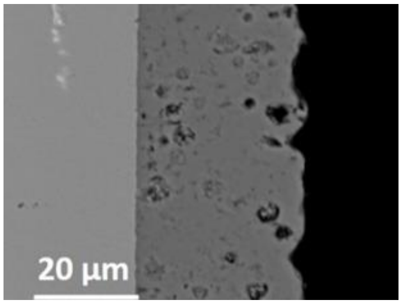

Fig. 5 Cross section of a converted layer with the Co-Mn precursor after 900°C x 2h sintering.

4.3 Summary

The electrical conductivities and CTEs of both $Ni_xFe_{3-x}O_4$ and $Mn_xCo_{3-x}O_4$ based spinel systems prepared via conventional solid-state processes were established. Optimal spinel compositions for cathode-side contact application were identified from those surveyed: $Ni_{0.85}Fe_{2.15}O_4$ ($\sigma = 14.5\ S\cdot cm^{-1}$ at 800°C, CTE = $12.10 \times 10^{-6}\ K^{-1}$) and $Mn_{1.2}Co_{1.8}O_4$ ($\sigma = 116\ S\cdot cm^{-1}$ at 800°C, CTE = $12.49 \times 10^{-6}\ K^{-1}$). Gas atomization was successfully utilized to process the alloy precursor powders with the desired composition and particle size that would lead to the formation of the promising spinels identified in this study. After thermal conversion (e.g., 900℃ x 2h) in air of the alloy precursor layer, a uniform and phase-pure spinel contact layer was achieved.

5. Task 3 – Demonstration and Validation of Contact Performance in Realistic Stack Environments

The utilization of gas-atomized alloy precursors is a promising approach to lowering the sintering temperature of the spinel contact layer and enhancing its performance. Based on the results from Task 2, the objective of this task is to critically evaluate and assess several gas-atomized Fe-Ni-Co and Co-Mn based alloy powders as the metallic precursor for reduced-temperature synthesis of the corresponding spinel layer for cathode-side contact application. The ASRs of the interconnect/contact/cathode test assemblies with the developed alloy powder derived contact layer were determined in a simulated cathode environment under both isothermal and cyclic exposure conditions. Cross-sectional examination of the tested assemblies were also be conducted with special attention paid to the interfacial regions between the interconnect and the contact as well as between the contact and the cathode.

5.1 Experimental Methods and Approaches

The interconnect alloy used in this study was either AISI 441 (441) with a composition of Fe-17.52Cr-0.31Mn-0.22Si-0.19Ti-0.014C (wt.%), Crofer 22 APU (Crofer) with a composition of Fe-22.74Cr-0.45 Mn-0.06Ti-0.11La-0,02Si-0.002C (wt. %) or ZMG232-G10 (ZMG) with a composition of Fe-24Cr-0.3Mn-2W-1Cu-0.25Zr-0.07La-0.1Al-0.1Si-0.02C (wt.%), which are Fe-Cr based ferritic alloys extensively studied for the interconnect application. The alloy sheet was cut into 15 × 15 × 0.5 mm coupons, which was subsequently was ground to 800 grits with SiC sand paper and ultrasonically cleaned in acetone. Some of the coupons had a 10-20 μm thick $(Mn,Co)_3O_4$ spinel layer as a protective coating. The $La_{0.8}Sr_{0.2}MnO_3$ (LSM) disks were used as the cathode. A number of atomized alloy precursors were used in this study for the $NiFe_2O_4$- or $MnCo_2O_4$-based spinel contact formation. A mixture of Co and MnO_2 powders prepared by manual mixing in a mortar and pestle was also included in evaluation in some case for comparison, which upon thermal conversion was expected to form the $MnCo_2O_4$ spinel layer. The Co and MnO_2 powders were 1.6 and 2-3 μm in diameter, respectively. An ink vehicle was mixed with the precursor powder to form the contact paste. The contact pastes was incorporated between the Crofer coupon and LSM cathode by screen-printing. Fig. 6 shows the test assembly configuration that simulated the interconnect/contact/cathode structure in a planar SOFC stack. A DC power supply was used to apply a constant current density of 250 $mA{\cdot}cm^{-2}$ across the assembly via one upper and one lower lead. A LabVIEW program was used in conjunction with a multi-channel Keithley 2700 multimeter to measure and record the voltage drop across each cell once every two minutes during testing via the other two leads. A compressive stress of 0.16 $kg{\cdot}cm^{-2}$ was applied during the test to simulate a stack environment. At the initial stage of the ASR testing, the test assemblies were heated to 900℃ and held for 2 h to thermally convert the contact precursors into a spinel layer. For isothermal ASR testing, the cell temperature was dropped to 800℃ and held at this temperature for 500-5000 h in air. For cyclic ASR testing, after sintering at 900°C the cell was then thermally cycled between 800°C (holding for 10 h) and 250°C (holding for 2 h), with a total of 200 cycles and a cumulative exposure of 2000 h at 800°C. The assembly ASR was monitored as a function of the holding time at 800°C.

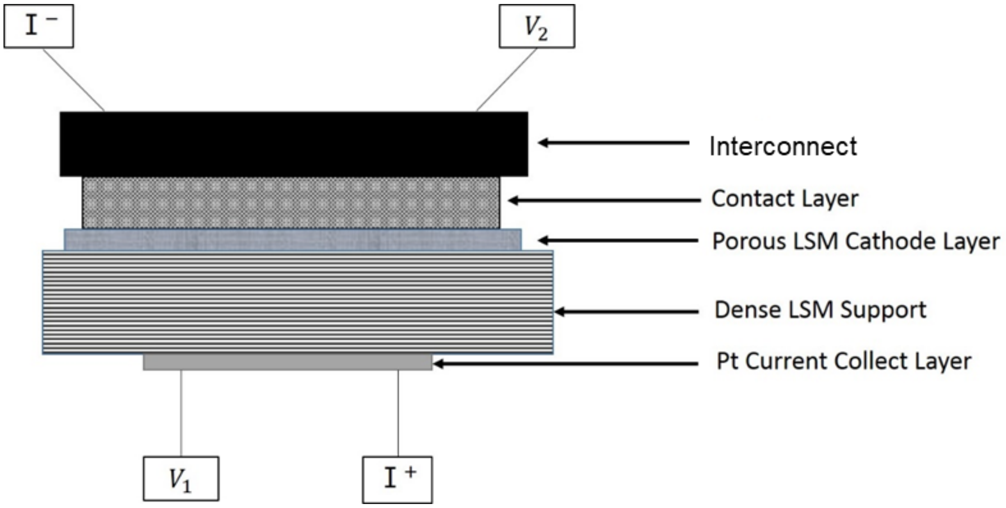

Fig. 6 Schematic drawing of a test assembly.

The ASR-tested assemblies were mounted, ground, and polished for assessing the cross-sectional microstructure of the contact layers and the potential interfacial interaction between the contact and adjacent components by SEM-EDS. The EDS line scans near the interconnect-contact and cathode-contact interfaces were obtained to identify possible interdiffusion and detrimental interaction. Special attention was paid to the thickness and quality of the Cr_2O_3 scale thermally grown on the interconnect alloy and the potential formation of a reaction layer between the Cr_2O_3 scale and contact layer. In addition, Cr migration throughout the cell was assessed for rough estimation of the Cr-blocking capability of the different contact materials.

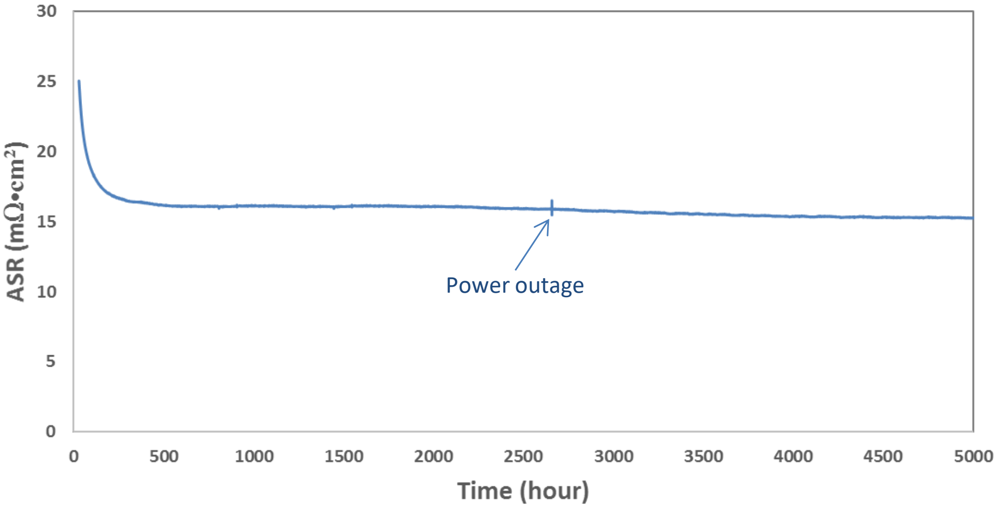

Fig. 7 ASR vs. time at 800°C in air during the 5000-h exposure for a 441/Fe-29.2Ni-16.5Co /LSM assembly.

5.2 Results and discussion

Fig. 7 shows the ASR change at 800°C for 5,000h in air for the 441/contact/LSM assembly with the alloy precursor composition of Fe-29.2Ni-16.5Co (in wt.%) . The ASR exhibited an initial rapid drop for the first couple of hundred hours, and then a slow, gradual decrease with a final ASR value stabilized at ~15 mΩ•cm^2. The initial ASR drop, similar to the previous results for the contact materials like noble metals, perovskites, or their composites between the interconnect and cathode could be related to the further sintering and microstructural homogenization of the contact layer during the initial ASR testing. The subsequent slow ASR decrease and final stabilization could be associated with the interdiffusion between the contact layer and the interconnect/cathode.

SEM/EDS analysis results on the polished cross-sections of the 5000-h ASR-tested assembly are shown in Fig. 8. As shown in Fig. 8(b), the contact layer after the long-term testing contained two phases, including the major $(Fe,Ni,Co)_3O_4$ spinel and the minor (Ni,Co)O phase. In addition, no Cr was detected in the contact layer, while the diffusion of Mn from the interconnect through the Cr_2O_3 scale to the contact layer was observed in Fig. 8(a). The Mn level was reasonably constant in the contact region adjacent to the Cr_2O_3 scale (about 20 μm) and then dropped quickly to essentially zero. Fig. 8(c) shows the EDS line scans with essentially no Cr detected in the cathode, implying that the Cr migration throughout the contact layer should not be not a concern for this alloy-derived contact layer, even though no coating was deliberately applied.

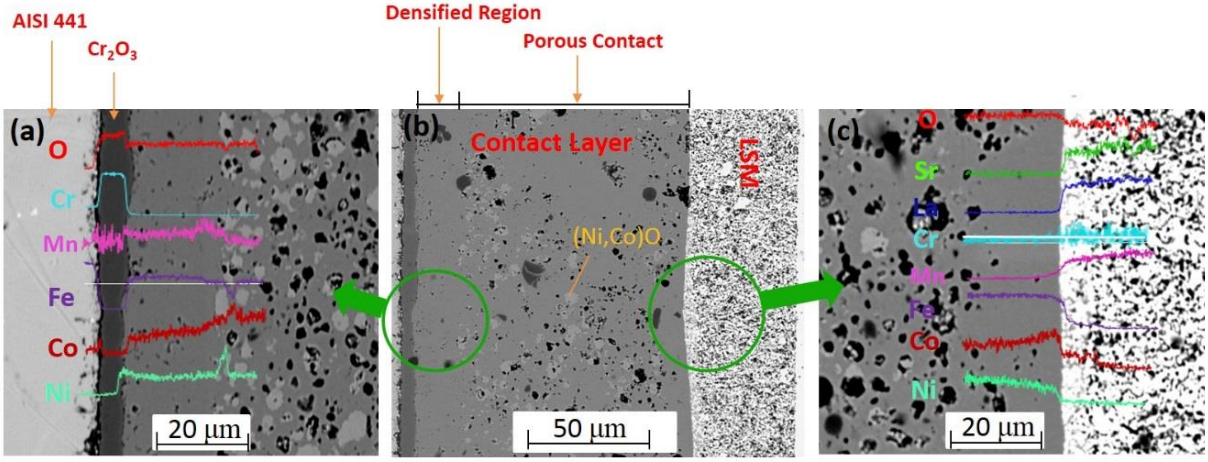

Fig. 8 Cross-sectional view of the 5000-h ASR tested assembly.

Fig. 9 shows the ASR change at 800°C for 1,000 h in air for the Crofer/contact/LSM assembly with several Co-Mn based alloy precursors (as listed in Table 4). Table 5 summarizes the initial ASR at the beginning of the test (R_i), the final ASR at the end of the test (R_f), and the average ASR degradation rates calculated for the initial and last 50 hours (i.e., DR_i and DR_f, respectively). Similar to the other coated interconnects or interconnect/contact/cathode assemblies synthesized via thermal conversion in air at a temperature of below 950°C [17-21], the R_i value of each cell in this study was also very low (≤ 4 mΩ·cm^2). All the test assemblies exhibited continuously increasing ASR during the test; however, overall, the ASR behaviors were exceptional with the R_f values of ≤ 7 mΩ·cm^2, compared to similar assemblies with the perovskite-type contact layer which typically had an ASR value of > 20 mΩ·cm^2 [22-25]. The assemblies with the alloy-derived contacts possessed a similar R_i value of about 1.8-2.2 mΩ·cm^2, which is roughly 50% lower than that with the Co+MnO_2 precursor. The DR_i value for the cell with the Co+MnO_2 precursor is 11.1 μΩ·cm^2/h, which is also much higher than those for the assemblies with the alloy precursors. This could be a result of the more porous contact microstructure for the cell with the mixed powder, which makes it easier for oxygen to reach the interconnect alloy surface in contact with the contact layer and subsequently faster Cr_2O_3 scale growth. For the assemblies with the contact layer formed with the Co-Mn and Co-Mn-Fe precursors, the DR_i values are similar, i.e., 3.3 and 3.5 μΩ·cm^2/h, respectively. Ce doping in Co-Mn-Fe-Ce led to a significantly lower DR_i, likely due to the reactive-element effect [26-31]]. Apparently, with the Ce dopant present in the contact layer, the Cr_2O_3 scale growth behavior on the Crofer surface might have been modified.

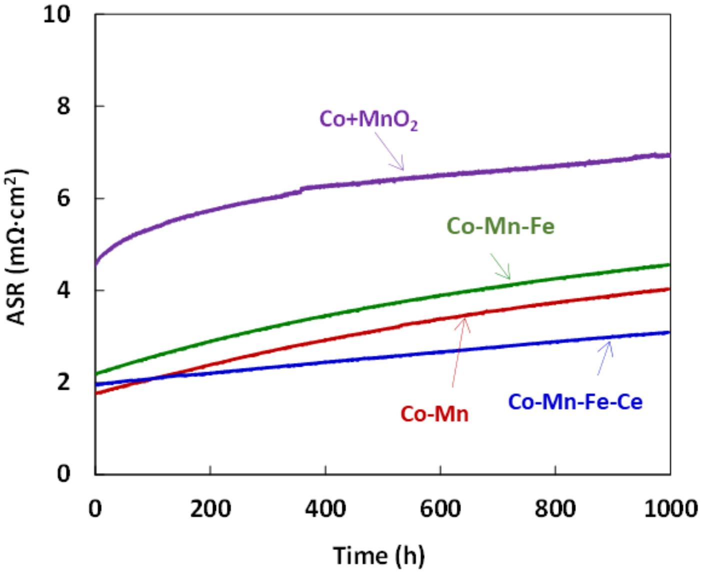

Fig. 9 ASR vs. time for Crofer/contact/LSM assemblies at 800°C in air (with different contact materials listed in Table 4).

While the ASR for all the assemblies increased continuously during the 1000-h exposure likely related to the further Cr_2O_3 scale growth on the interconnect, the ASR degradation rate decreased with time for all of them as the Cr_2O_3 scale growth was expected to slow down with time. Furthermore, DR_f was very similar for Co+MnO_2, Co-Mn, and Co-Mn-Fe derived contacts, i.e., about 1.3-1.4 μΩ·cm^2/h, implying that the Cr_2O_3 scale growth was similar fore these assemblies after the 1000-h exposure at 800°C. On the other hand, the Ce addition to the alloy powder lowered the DR_f and R_f noticeably (i.e., to about 1.0 μΩ·cm^2/h and 3.1 mΩ·cm^2/h, respectively), further confirming the beneficial influence of Ce addition into the contact layer in altering the chromia scale growth behavior on the Crofer alloy. Using the DR_f for the cell with the Ce-doped spinel contact layer as the ASR degradation rate for subsequent exposure, it can be estimated that the cell ASR will be about 43.1 mΩ·cm^2 after 40,000 h operation at 800°C (as expected for the stationary SOFC application). This is still much lower that the acceptable ASR target for the interconnect (~100 mΩ·cm^2). Furthermore, since the assembly degradation rate is expected to further decrease slowly over time, it can be concluded that the Ce-doped spinel derived from the multi-component alloy is very promising for long-term cathode-side contacting application.

Table 5 Initial ASR (R_i), final ASR after the 1000-h testing (R_f), ASR degradation rate during the initial 50 h (DR_i), and ASR degradation rate during the last 50 h (DR_f)

	Co-Mn	**Co-Mn-Fe**	**Co-Mn-Fe-Ce**	**Co+MnO$_2$**
R_i (mΩ·cm^2)	1.8	2.2	2.0	4.6
R_f (mΩ·cm^2)	4.0	4.6	3.1	7.0
DR_i (μΩ·cm^2/h)	3.3	3.5	1.5	11.1
DR_f (μΩ·cm^2/h)	1.4	1.3	1.0	1.4

Fig. 10 shows the cross-sections of the tested assemblies after 1000-h isothermal exposure at 800°C in air. From the left to the right, the components were Crofer, contact layer, porous LSM cathode, and dense LSM support for each assembly, as indicated in Fig. 10(a). A continuous, uniform and crack-free contact layer with a thickness of 90~100 μm was successfully formed in each assembly, indicating that these thermally-converted contact layers exhibited exceptional CTE match and good bonding with the adjacent components. Also, based on SEM/EDS analysis, minimal interdiffusion was observed between the alloy-derived contact layer and cathode. Furthermore, as shown in Fig. 11(a), no Cr was detected in the LSM cathode or the contact region close to the cathode for the assemblies with the alloy contact precursors, further confirming the effectiveness of the Co-Mn based alloy-derived spinel contact layer in blocking Cr migration to the cathode. However, as shown in Fig. 11(b), the EDS line of Cr in the cell with the Co+MnO$_2$ contact precursor fluctuated in the porous LSM cathode noticeably, implying that the porous contact layer likely allowed some Cr species migrated to the cathode. Since the cathode poisoning could occur eventually if Cr reaches the LSM cathode, the alloy-derived contact layer is clearly advantageous in this regard.

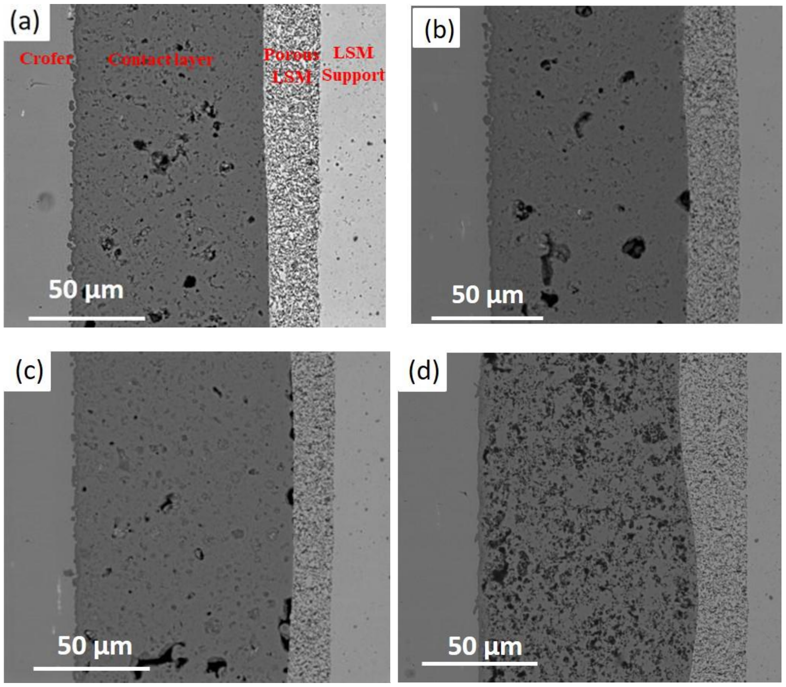

Fig. 10 SEM Cross-sectional images of the test assemblies with different contact precursors: (a) Co-Mn, (b) Co-Mn-Fe, (c) Co-Mn-Fe-Ce, and (d) Co+MnO$_2$.

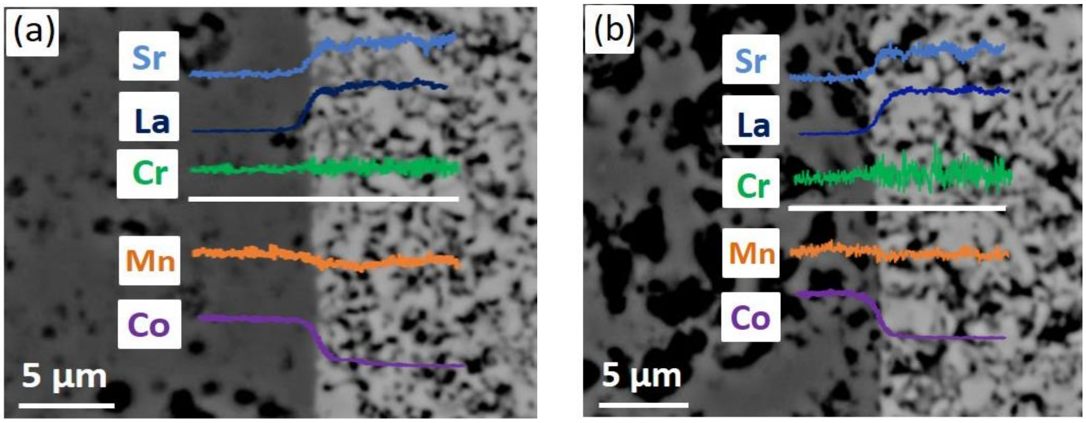

Fig. 11 SEM cross-sectional view with the superimposed EDS line scans near the contact-cathode interface for the assemblies with different contact precursors: (a) Co-Mn and (b) Co+MnO_2.

The ASR for the test assemblies with three contact materials as a function of time at 800°C in air for 2000 h during cyclic exposure is shown in Fig. 12. Reactively-sintered $(Mn,Co)_3O_4$ (MCO) spinel derived from an alloy precursor was chosen due to its reasonable conductivity and well-matched CTE. LSM was included in the evaluation for comparison because of its widespread use in SOFCs along with a well-matched CTE and high conductivity, while $La(Mn_{0.45}Co_{0.35}Cu_{0.2})O_3$ (LCC10) was chosen due to its reasonably-matched CTE and enhanced sinterability [32,33]. Overall, the ASR for the assembly with the Co-Mn alloy derived MCO contact was the lowest and most stable. At the end of the test, the ASRs for the assemblies with MCO, LSM, and LCC10 were 8.24, 13.3, and 16.9 $m\Omega\cdot cm^2$, respectively. Also, a sharp increase in ASR occurred during the first 50 h (i.e., during the first 5 cycles) for the LSM and LCC10 samples. This marked increase implies that thermal cycling may have induced cracking in the contact layer which leads to a decreased contact area and subsequently a higher ASR.

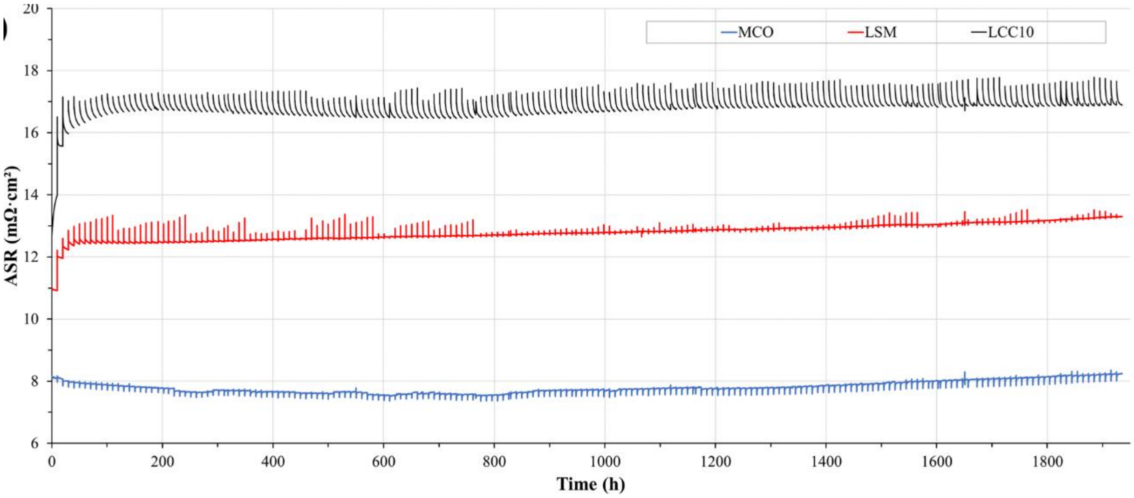

Fig. 12 ASR as a function of exposure time at 800°C in air for thermally cycled test assemblies with the MCO, LSM, and LCC10 contacts.

The microstructure of each cycled test assembly along with the interactions between the assembly components was examined, as shown in Fig. 13. Each contact layer appeared well-sintered after testing with a reasonable porosity level. The LSM and LCC10 contact microstructure, however, showed severe cracking, as shown in Figs. 13(b) and (c), respectively. Cracks proceeded through roughly half of the LCC10 contact layer and through the majority of the LSM contact layer, predominantly along the contact/cathode interface. Vertical cracking through the contact layer was also observed, which was more common in the LCC10 contact and was only detected in the LSM contact occasionally. Although vertical cracking likely does not contribute to an ASR increase because the contact area is not reduced, these cracks could serve as open pathways for volatile Cr species to migrate to the cathode which can cause “chromium poisoning”. In contrast, not a single crack was detected in the assembly with the MCO contact after cyclic test, which is consistent with the lowest ASR value for this assembly. The superior resistance to cycle-induced cracking for the MCO contact can be explained by the fact that the MCO contact has an essentially same CTE as that of the MCO coating or the LSM cathode. EDS analysis of the interconnect/coating/cathode interfaces in Fig. 13 indicated no significant diffusion between the coating and contact for the LSM- and MCO-contacted assemblies. The LCC10-contacted assembly, however, showed that Cu had fully diffused from the contact layer into the coating. At the contact/cathode interface, no significant diffusion was observed for any of the tested assemblies.

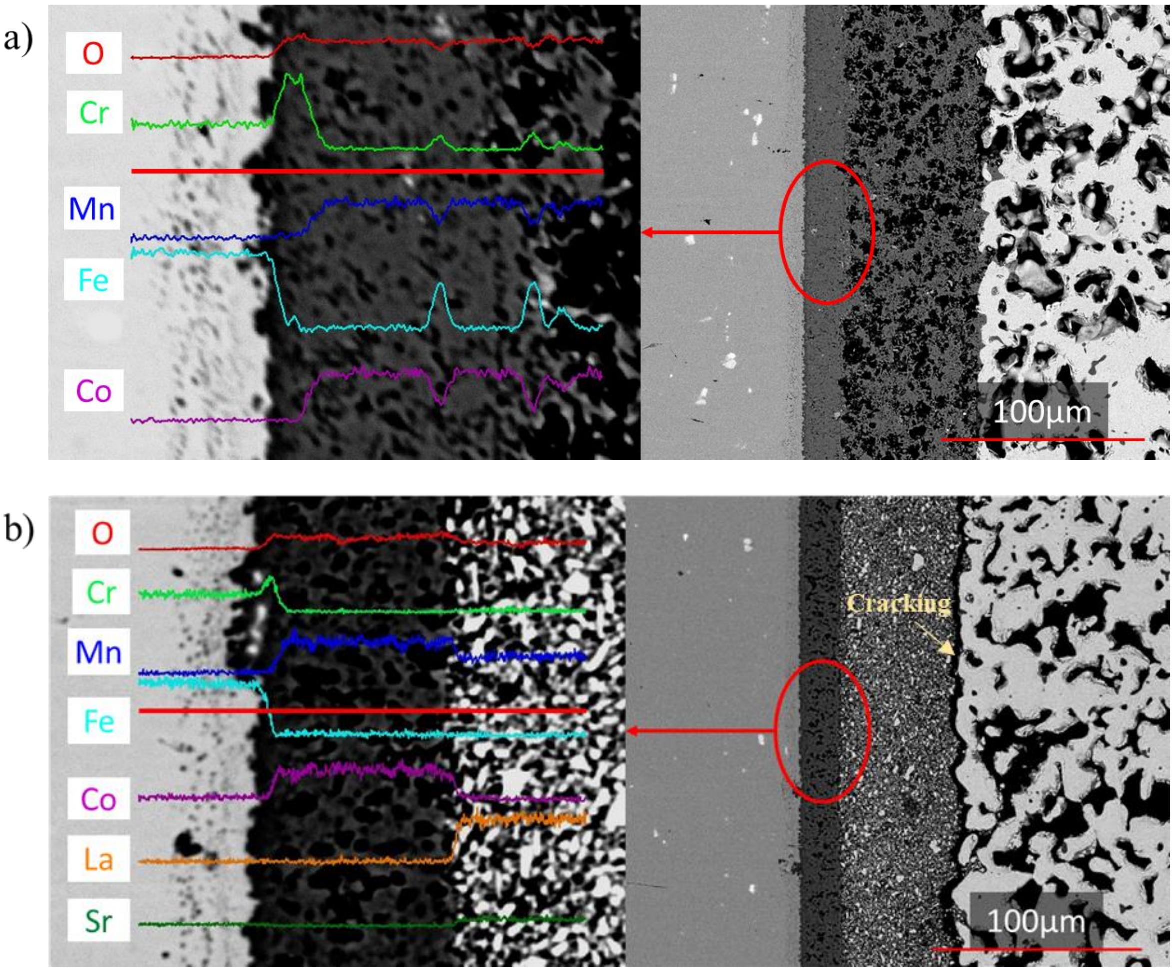

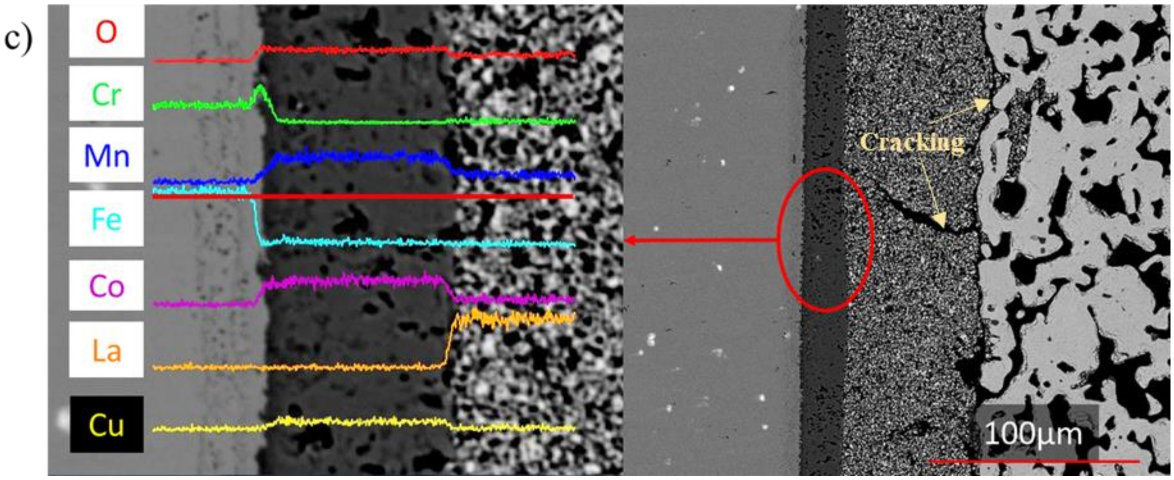

Fig. 13 Microstructures of the tested assemblies with different contact materials: (a) MCO, b) LSM, and c) LCC10, superimposed with the EDS results near the interconnect/coating/contact interface.

5.3 Summary

Different gas atomized alloy precursor materials were selected for synthesis of the $NiFe_2O_4$- or $MnCo_2O_4$-based contact layer between the interconnect and LSM cathode via the reactive sintering process. All the test assemblies exhibited exceptional electrical performance during the ASR test as well as good thermal and chemical compatibility with the adjacent cell components, confirming that the Ni-Fe and Co-Mn alloy derived spinel contact was promising for the interconnect-cathode contact application. While Fe addition into the Co-Mn alloy powder had no beneficial effect on the electrical performance, Ce doping led to the lowest cell ASR and ASR degradation rate as a result of slower Cr_2O_3 scale growth and better scale adhesion. In addition to the ASR improvement, the utilization of a pre-alloyed powder as the spinel contact precursor offered several other advantages including elimination of the powder mixing step, formation of more compositionally-uniform contact, and excellent Cr-blocking capability. Furthermore, a reactive-element doped spinel layer was readily achieved via the addition of the desired element into the precursor alloy during the alloy-making step.

6. Task 4 Further Cost Reduction and Commercialization Assessment

One major objective of this task is to explore two different approaches to lowering the overall stack cost, including (1) reactive synthesis of uniform, dense $(Mn,Co)_3O_4$ (MCO) spinel coatings with the atomized alloy powder precursor with unique particle size, size distribution, and chemical composition to reduce the interconnect coating cost and (2) co-sintering of the alloy precursor derived MCO-based dense spinel coating and porous contact layer under the SOFC stack firing condition.

Also, a preliminary cost analysis was conducted to assess the effectiveness of the incorporation of coating/contact co-sintering during initial stack firing on the total stack cost reduction. The feasibility of process scale-up was assessed for potential implementation of the new material/process in the stack manufacturing facilities.

6.1 Experimental Methods and Approaches

Three ferritic stainless steels were used as substrates: Crofer, ZMG, and AISI 441. Each 1 mm thick substrate was sectioned into 15 mm × 15mm coupons, polished up to 600-grit with SiC grinding paper, and subsequently cleaned with acetone prior to coating. Metallic Co-Mn powder precursor and an ink vehicle were mixed to form a paste. The precursor slurry was then applied to the interconnect coupons via screen printing. Since all sides of the coupon needed spinel coverage, the precursor coating was dried prior to screen printing on the other side and the 1 mm thick substrate edges were painted on with a thickened version of the same paste. By optimizing the powder characteristics (size, size distribution) and the alloy precursor composition, a dense spinel coating was achieved after the thermal conversion. Both Ce-free an Ce-doped Co-Mn precursor powders were then used to synthesize the dense MCO and Ce-doped MCO coatings. Once the green coatings were applied, the coated substrates were reactively sintered at 900°C for 2 h. Likewise, the uncoated substrates were also subjected to a 2 h 900°C heat treatment to simulate stack firing conditions and serve as a reference. After all the substrates were heat treated, the samples were hung from alumina rods and oxidized in 800°C air for 6,000 h continuously. After oxidation, the furnace was cooled to room temperature, and the samples weighed on a scale with 0.1 mg accuracy. The oxidation behaviors of bare and coated samples were compared.

Some full-size ZMG/coating/contact/LSM assemblies with an Co-Mn based alloy precursor contact layer applied between a Co-Mn alloy precursor-coated ZMG alloy plate and an LSM plate (both plates had ~ 80 mm x 80 mm square cross section) were prepared for co-sintering as well as ASR testing under both isothermal and cyclic exposures.

For in-stack testing with the co-sintered coating/contact layers, each of the ZMG current collector plate and the LSM end plate of an all-ceramic stack were applied with a respective Co-Mn alloy precursor layer. After two precursor layers were contacted to form a stack attached with the ZMG plate, the stack was sintered at 900°C for 2 h in air for testing.

An analysis of both raw material and process-related costs was conducted by comparing the new alloy precursor-based approach with the conventional ones for the both cathode-side contact layer and interconnect coating applications. The cost estimation is based on a 270 kW

SOFC power system sized for ground-based distributed generation, which was extensively studied by Weimar et al. [34]. The interconnect coating was also included in this analysis, as the alloy precursor-based approach can be readily adapted for dense interconnect coating synthesis via controlling the alloy precursor powder size/composition/packing as well as the sintering conditions. Furthermore, co-sintering of the contact layer and interconnect coating during initial stack firing/operation could eliminate several processing steps and lead to significant overall stack cost reduction.

6.2 Results and Discussion

The current industrial practice for the MCO coating is either atmospheric plasma spray (APS) (developed by Forschungszentrum Jülich) or reduction-reoxidation with a Co oxide and Mn carbonate mixture or with an MCO spinel powder (developed by PNNL and commercialized by NexTech). To reduce the MCO coating cost and minimize the warpage of the alloy plate during coating fabrication, the EARS process was utilized to reactively sinter a dense MCO spinel coating on the ferritic alloy with a MCO-forming precursor screen printed onto the alloy substrate. By controlling the composition, shape, size, and size distribution of the CO-Mn based alloy powders, a dense spinel layer was obtained after thermal conversion at 900°C for 2 h in air. Fig. 14 compares the microstructures of TTU’s MCO coating (Fig. 14f) and the similar coatings from different groups (Fig. 14a-e). Obviously, the quality of the reactively sintered coating was superior, with very high uniformity and low porosity. Some of the unique process advantages of TTU’s alloy precursor-derived MCO coating are low processing temperature (≤ 900°C) and no need of a reduction treatment in H_2-containing environment.

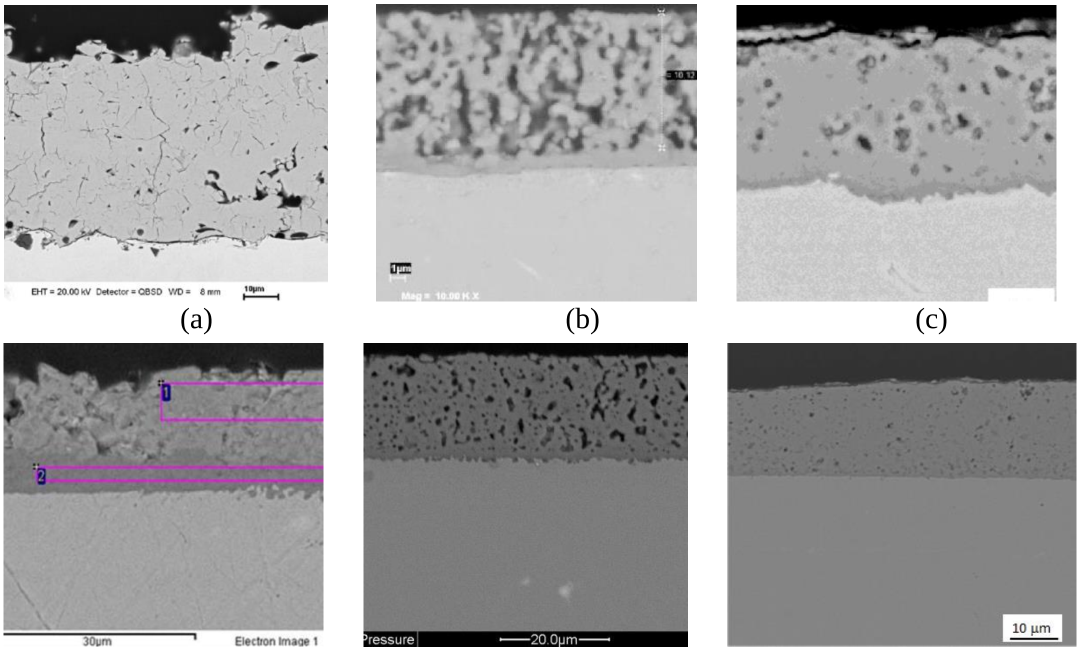

(a) (b) (c)

(d) (e) (f)

Fig. 14 Cross-sectional view of the MCO coatings from different groups: (a) Jülich; (b) PNNL; (c) NexTech; (d) FuelCell Energy; (e) the industrial partner; and (f) TTU.

The mass gains of the bare, MCO-coated, and Ce-doped MCO-coated ZMG and Crofer are shown in Fig. 15. For each of the 441 substrates, significant mass loss was observed due to major spallation of the substrate coatings and oxide scales. For this reason, the mass gain data for the 441 substrates is not included in Fig. 15. However, the mass gain data for the Ce-doped MCO-coated, MCO-coated, and uncoated samples are -6.4 ± 0.4, -7.06 ± 0.03, and 0.3 ± 0.3 mg cm^{-2}, respectively. For both the ZMG and Crofer samples, the uncoated substrates exhibited the greatest weight gain attesting to the improved oxidation resistance of the MCO coating. Among the coated samples, the Ce-doped coatings exhibited a smaller mass gain after oxidation compared to the undoped samples. Although the standard deviation for the doped samples is quite large especially for the Crofer sample, there seems to be a positive relationship between Ce addition and improved oxidation resistance. The effect of Ce addition into the MCO coating seems to be more pronounced for the ZMG alloy. This increase may be due to the lower La concentration in the ZMG alloy compared to Crofer. Therefore, the Ce addition into the coating would produce a more pronounced oxidation resistance improvement because of a stronger reactive element effect.

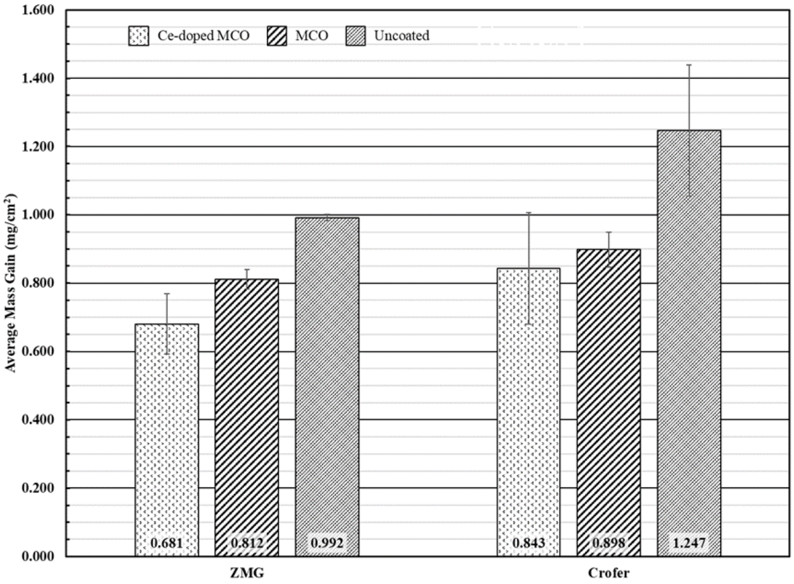

Fig. 15 Mass gain of bare, MCO-coated, and Ce-doped MCO-coated ZMG and Crofer after 6000 h oxidation at 800°C in air.

Fig. 16 shows a cross-sectional image of the co-sintered coating/contact dual-layer structure. Obviously, a dense spinel coating on the ferritic alloy side and a porous spinel contact between the coated alloy and LSM cathode was achieved. Fig. 17 shows the ASR of the full-size ZMG/coating/contact/LSM assembly vs. time during the initial 250-h exposure and subsequent 12 deep cycles (each cycle consists of holding for 10 h at 800°C, cooling to room temperature and then re-heating to 800°C). Overall, the ASR was very low (i.e., about 3-4 $m\Omega.cm^2$), which is likely due to the co-sintering process used to sinter the coating and contact layer simultaneously, which led to low interfacial resistance at the alloy-coating and coating-contact interfaces. During severe thermal cycling between 800°C and room temperature, the ASR maintained a relatively stable value, indicating that the effect of thermal cycling on its ASR performance was minimal.

This is clearly due to the almost perfect match in CTE between the different layers in the assembly.

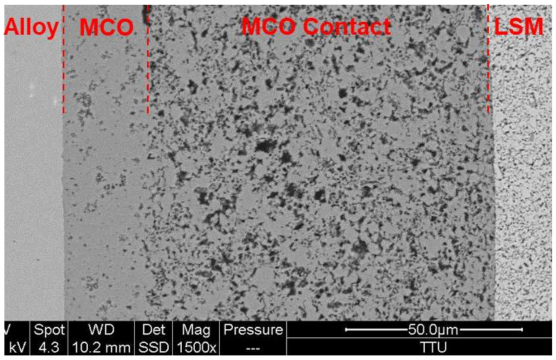

Fig. 16 Cross-sectional view of a co-sintered coating/contact dual-layer structure between the ferritic alloy ZMG and LSM cathode plates.

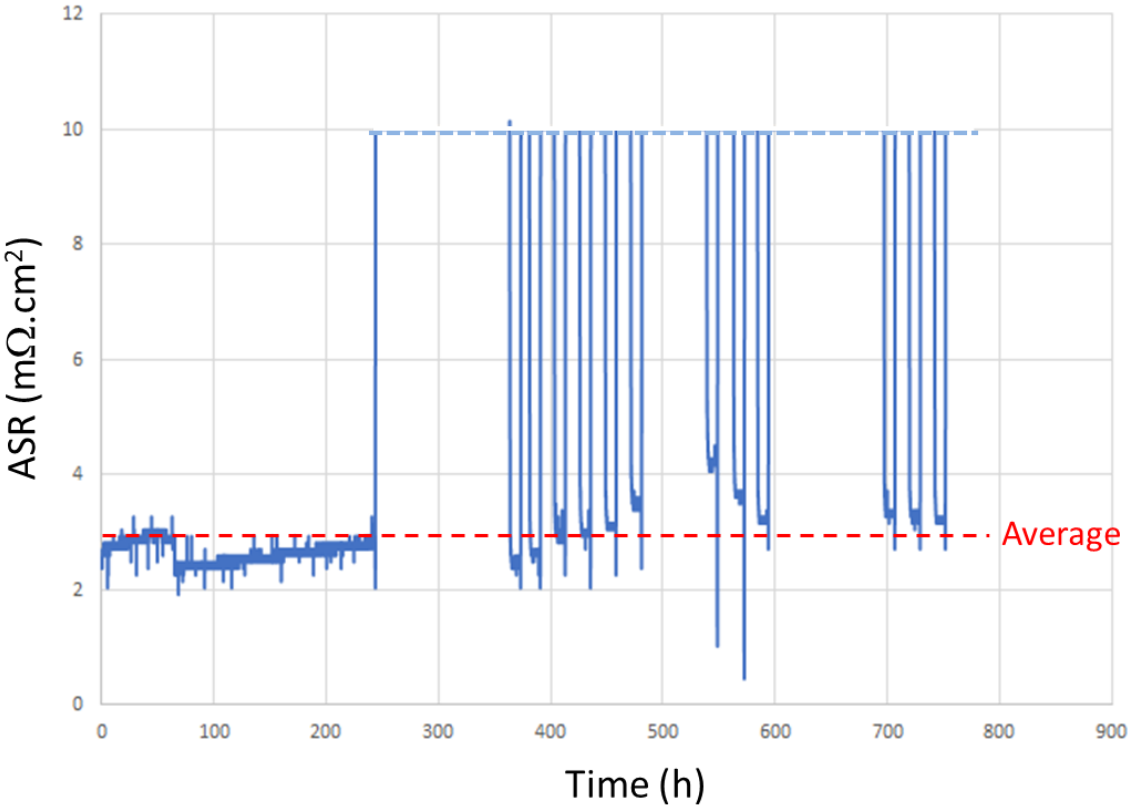

Fig. 17 ASR as a function of time during isothermal and cyclic exposures at 800°C in air for a full-size ZMG/coating/contact/LSM assembly co-sintered at 900°C for 2 h in air.

Fig. 18 shows the overall view of the sintered stack with the ZMG alloy plate incorporating the all-ceramic stack supplied by the industrial partner, the machined ZMG alloy end plates, and the metallic contact and coating precursors prepared at TTU. It appears that the MCO coating on the ZMG end plates was quite smooth and uniform and no obvious defects could be detected with naked eyes. Moreover, the ZMG end plates were bonded to the stack adequately and the bonded assembly was rigid enough for aggressive handling. Currently, the industrial partner is testing TTU's materials in their full-size stack assembly to increase the TRL level of the co-sintering technology. It should be noted that the testing has been delayed due to some scheduling issues.

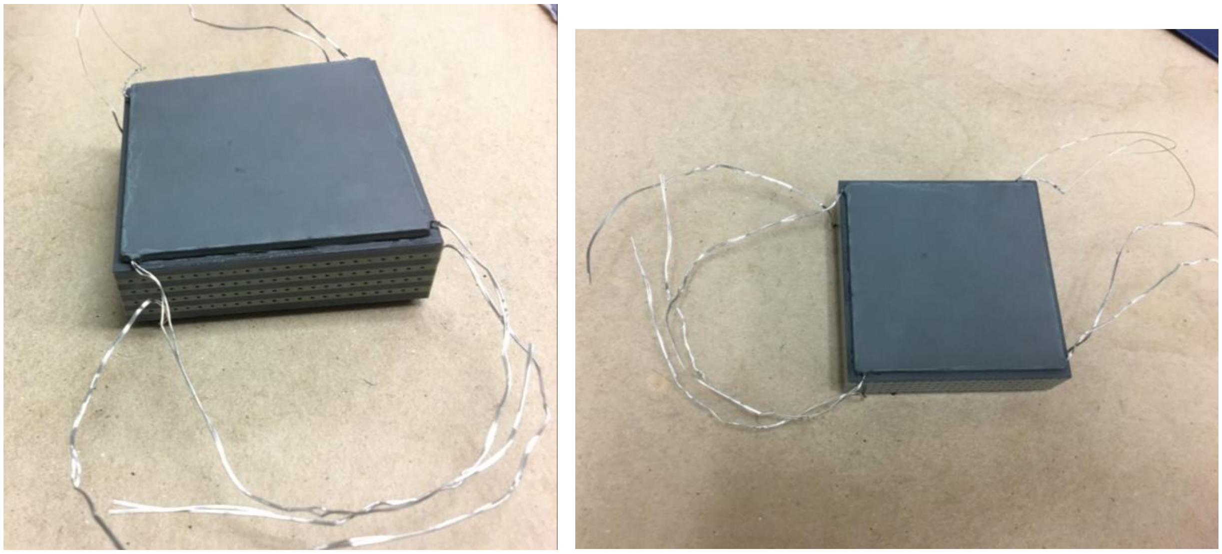

Fig. 18 Digital images of a sintered stack assembly.

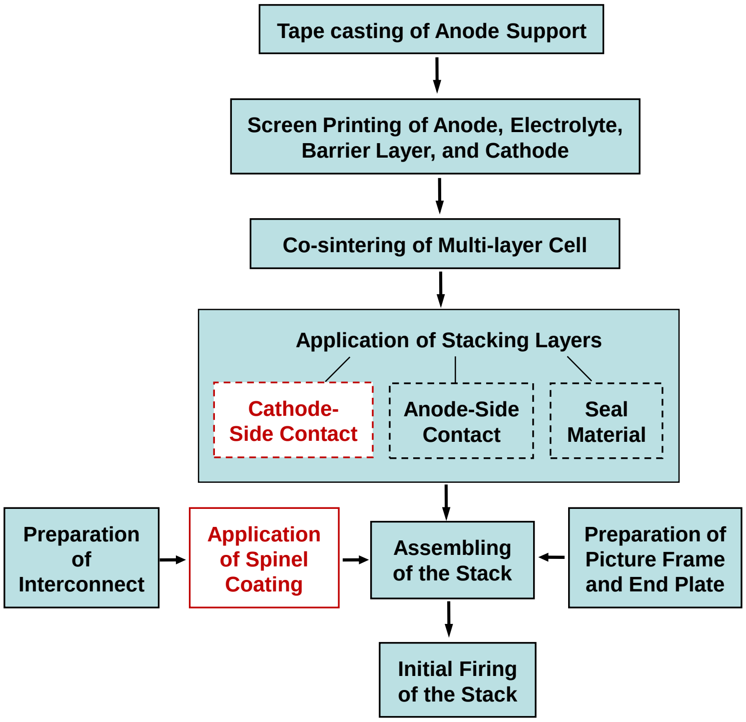

Fig. 19 Flow chart showing key SOFC stack manufacturing processes.

The manufacture of SOFC stacks is quite complicated, involving numerous processing steps [34-36]. To demonstrate the impact of TTU's innovative concept, a simplified SOFC manufacturing flow chart is given in Fig. 19, which incorporates one of the leading industrial technologies for single-cell fabrication – the tape casting-screen printing-cosintering (TSC) process. The new alloy precursor-based approach developed under this project will mainly impact the application of both the cathode-side contact layer and interconnect coating. The dedicated contact sintering step can be eliminated for the cathode-side contact application (Fig. 20), while both high-temperature reduction and re-oxidation steps can be avoided for the interconnect coating application (Fig. 21). The conversion/sintering of these layers can instead be achieved during initial stack start-up/operation.

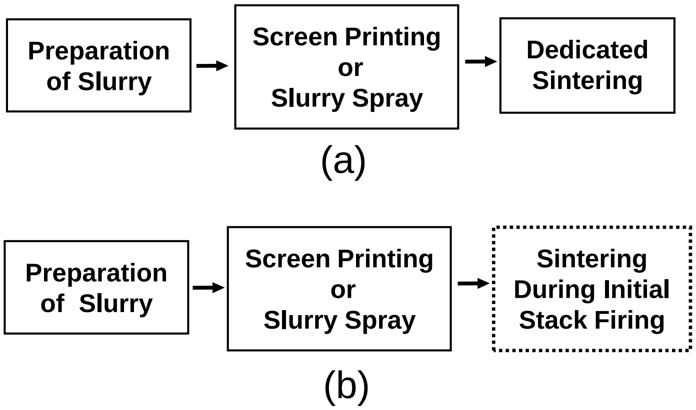

Fig. 20 Process steps for contact layer application: (a) conventional and (b) new approach.

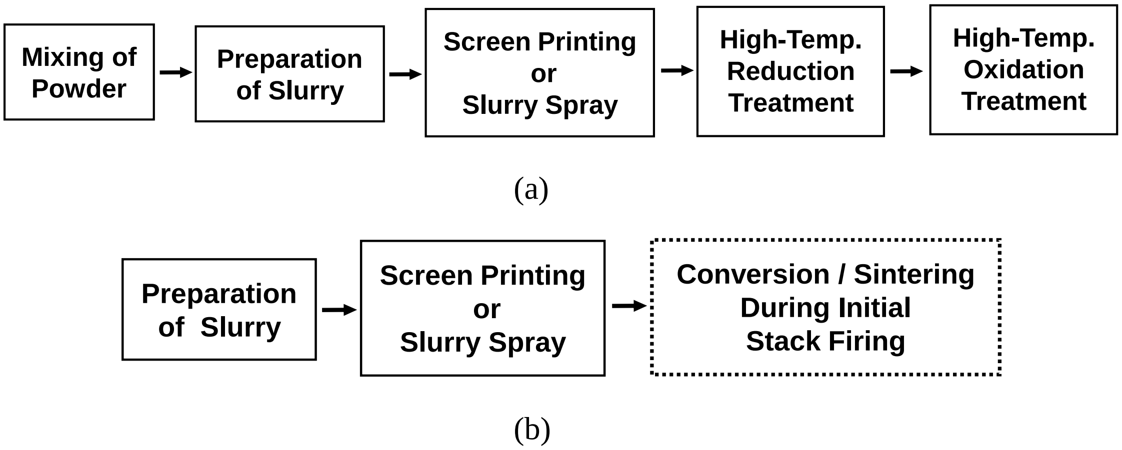

Fig. 21 Process steps for spinel coating application: (a) conventional and (b) new approach.

Cost analysis is conducted by comparing the new and conventional approaches, from both material and process perspectives. As shown in Table 6, the material cost with TTU's new alloy precursor approach is similar to that with the conventional one, as the same Co-Mn based spinel contact/coating composition will be employed. Also, only one powder needs to be prepared and the powder mixing step is eliminated with the new alloy approach. According to the quote from an industrial vendor, the cost of the alloy powder is $90/kg, which is much lower than that of Ag powder ($1,100/kg) [34] or LSM powder ($700/kg). The annualized capital, electricity, operation and maintenance (O&M), and labor are also estimated and compared for the two approaches, as detailed in Table 6. The data for the conventional approach was derived from Ref. 34; however, instead of Ag, LSM was selected as the contact in the current cost study. The lower process-related costs for the alloy precursor approach are due to the utilization of low-cost screen printing or slurry spray for the precursor application as well as the elimination of some processing step(s) as illustrated in Figs. 20 & 21. For the conventional approaches, the high-temperature vacuum-tight furnaces can be quite expensive (~$500,000 each), and the process gas and the electricity consumed during annealing will add the cost. Moreover, a milling machine is needed to mix the precursor powders for the reduction-oxidation synthesis of interconnect coating, while no such mixing will be required for the alloy powder.

Table 6 Production costs of contact layer, interconnect coating, and stack per system

Cost System		Material Cost ($)	Annualized Capital and O&M ($)				Total ($)	Stack Cost Reduction
			Capital	Electricity/Gas	O&M	Labor		
Contact Layer	Conventional	792	769	12	62	125	1,760	6.1%
	New	131	59	6	16	25	237	
Interconnect Coating	Conventional	160	846	55	65	149	1,275	4.5%
	New	44	59	6	16	25	150	
Stack	Conventional	13,285	8,122	251	1,684	1,806	25,148	10.6%
	New	12,493	6,625	196	1,589	1,582	22,485	

From Table 6, a stack cost reduction of 6.1% can be achieved, if the new alloy precursor concept is implemented for cathode-side contact application. An additional 4.5% cost reduction is expected, if interconnect coating can also be synthesized using TTU's alloy precursor powder, and co-sintering of the interconnect coating and the contact layer can be realized during initial stack firing. This leads to a total stack cost saving of around 10.6%, if both cathode-side contact and interconnect coating are considered.

Since low-cost processes such as screen printing are utilized in the contact/coating precursor application and no reduction heat treatment is needed for the coating formation, the developed technology can be readily implemented at the industrial partner's manufacturing facilities with no additional capital investment needed.

6.3 Summary

By optimizing the particle size, size distribution, and composition of the alloy precursor powder, a dense MCO spinel coating was successfully synthesized on the interconnect alloy via environmentally-assisted reactive sintering. Furthermore, the beneficial effect of Ce doping in the MCO coating on the oxidation performance of several interconnect alloys were demonstrated. To further reduce the stack processing cost, co-sintering of MCO-based spinel coating and contact layer was explored using the optimized MCO coating/contact precursor layers applied between the full-size ZMG current collector and LSM stack end plate to form full-sized ZMG/coating/contact/LSM assembly. Thermal cycling did not negatively affect the ASR performance of the full-size assembly. The stack attached with the coated ZGM plates is being tested by the industrial collaborator to assess the performance of the developed co-sintered coating/contact layers. A preliminary cost analysis indicates a total stack cost reduction of around 10.6% with the implementation of co-sintering of the coating and the contact layer during initial stack firing using the developed alloy powder precursors. Since low-cost processes such as screen printing are utilized in the precursor application and no reduction heat treatment is needed for the coating formation, the developed technology can be readily implemented at the industrial partner's manufacturing facilities with no additional capital investment needed.

7. List of Publications Based on This Work

Journal Papers:

1. D.A. Chesson and J.H. Zhu, “Effect of spinel stoichiometry on reaction layer formation between $(Mn,Co)_3O_4$ and Cr_2O_3”, to be submitted to Solid State Ionics, 2023.
2. J.H. Zhu, D.A. Chesson, and Y. T. Yu, “$(Mn,Co)_3O_4$-based spinels for SOFC interconnect coating application: a review”, Journal of The Electrochemical Society, 168, p.114519, 2021.
3. D.A. Chesson and J.H. Zhu, “Effect of off-stoichiometry on electrical conductivity in Ni-Fe and Mn-Co spinel systems”, Journal of The Electrochemical Society, 167(12), p.124515, 2020.
4. Y.T. Yu, J.H. Zhu, and B.L. Bates, “Conductive spinels derived from Co–Mn based alloy precursor for SOFC cathode-side contact application”, International Journal of Hydrogen Energy, 45, 27745-27753, 2020.
5. L.P. Wang, W. Yang, Z.B. Ma, J.H. Zhu, and Y.T. Li, “First-principles study of chromium diffusion in the ferritic Fe-Cr alloy”, Computational Materials Science, 181, p.109733, 2020.
6. Y.T. Yu, J.H. Zhu, and B.L. Bates, “Effect of precursor materials on the performance of the $NiFe_2O_4$-based spinel layer for SOFC cathode-side contact application”, Solid State Ionics, 324, p. 40 (2018).
7. Y.T. Yu and J.H. Zhu, “Reactive sintering of a $CoFe_2O_4$ coating on ferritic stainless steels for SOFC interconnect application”, Journal of The Electrochemical Society, 165, p. F297 (2018).

Theses and Dissertations

1. J. Hayes, “The Performance of Mn-Co Spinel Cathode-Side Contact Layer and Interconnect Coating for Solid Oxide Fuel Cell Application”, MS. Thesis, 2021.
2. D.A. Chesson, “Effect of Off-Stoichiometry on Electrical Conductivity in Ni-Fe and Mn-Co Spinel Systems for Solid Oxide Fuel Cell Interconnect Coating and Contact Layer Applications”, Ph.D. Dissertation, 2021.
3. Y.T. Yu, “The Performance of Spinel-Based Interconnect Coating and Cathode-Side Contact Layer for Solid Oxide Fuel Cell Application”, Ph.D. Dissertation, March, 2020.
4. T.K. Fang, “Synthesis and Evaluation of Manganese Cobalt Spinel”, MS. Thesis, 2020.

8. References

1. J. H. Zhu and H. Ghezel-Ayagh, “Cathode-side electrical contact and contact materials for solid oxide fuel cell stacking: a review,” *Int. J. Hydrog. Energy*, vol. 42, no. 38, p. 24278, 2017.
2. M. Shenand P. Zhang, “Progress and challenges of cathode contact layer for solid oxide fuel cell”, *Int. J. Hydrog. Energy*, vol. 45, p. 33876, 2020.
3. N. Shaigan, W. Qu, D.G. Ivey, and W.X. Chen, “A review of recent progress in coatings, surface modifications and alloy developments for solid oxide fuel cell ferritic stainless steel interconnects”, *J. Power Sources*, vol. 195, p.1529, 2010.
4. Z.G. Yang, “Recent advances in metallic interconnects for solid oxide fuel cells”, *Int. Mater. Rev.*, vol. 53 p. 39, 2008.
5. Z.G.Yang, G.G. Xia, G.D. Maupin, and J.W. Stevenson, “Conductive protection layers on oxidation resistant alloys for SOFC interconnect applications”, *Surf. Coat. Technol.*, vol. 201, p. 4476, 2006.
6. Z.G. Yang, G.G. Xia, and J.W. Stevenson, “$Mn_{1.5}Co_{1.5}O_4$ spinel protection layers on ferritic stainless steels for SOFC interconnect applications”, *Electrochem. Solid State Lett.*, vol. 8, p. A16, 2005.
7. Z.G. Yang, G.G. Xia, S.P. Simner, and J.W. Stevenson, “Thermal growth and performance of manganese cobaltite spinel protection layers on ferritic stainless steel SOFC interconnects”, *J. Electrochem. Soc.*, vol. 152, p. A1896, 2005.
8. M. Stanislowski, J. Froitzheim, L. Niewolak, W.J. Quadakkers, K. Hilpert, T. Markus, and L. Singheiser, “Reduction of chromium vaporization from SOFC interconnectors by highly effective coatings”, *J. Power Sources*, vol. 164, p.578, 2007.
9. J.H. Zhu, D.A. Chesson, and Y.T. Yu, “$(Mn,Co)_3O_4$-based spinels for SOFC interconnect coating application”, *J. Electrochem. Soc.*, vol. 168, p. 114519, 2021.
10. D.A. Chesson and J.H. Zhu, “Effect of off-stoichiometry on electrical conductivity in Ni-Fe and Mn-Co spinel systems”, *J. Electrochem. Soc.*, vol. 167, p. 124515, 2020.
11. A.T. Nelson, J.T. White, D.A. Andersson, J.A. Aguiar, K.J. McClellan, D.D. Byler, M.P. Short, and C.R. Stanek, “Thermal expansion, heat capacity, and thermal conductivity of nickel ferrite ($NiFe_2O_4$)”, *J. Am. Ceram. Soc.*, vol. 97, p. 1559, 2014.
12. A. Topcu, B. Öztürk, and Ö.N. Cora, “Performance evaluation of machined and powder metallurgically fabricated Crofer® 22 APU interconnects for SOFC applications”, *Int. J. Hydrog. Energy*, vol. *47*, p. 3437, 2022.
13. A. Petric, Anthony and L. Hang , “Electrical conductivity and thermal expansion of spinels at elevated temperatures”, *J. Am. Ceram. Soc.*, vol. 90., p. 1515, 2007.
14. A. Rousset, C. Tenailleau, P. Dufour, H. Bordeneuve, I. Pasquet, S. Guillemet-Fritsch, V. Poulain, and S. Schuurman, “Electrical properties of $Mn_{3-x}Co_xO_4$ ($0\leq x\leq 3$) ceramics: an interesting system for negative temperature coefficient thermistors”, *Int. J. Appl. Ceram. Technol.*, vol. 10, p. 175, 2013.

15. H. Bordeneuve, S. Guillemet-Fritsch, A. Rousset, S. Schuurman, and V. Poulain, “Structure and electrical properties of single-phase cobalt manganese oxide spinels $Mn_{3-x}Co_xO_4$ sintered classically and by spark plasma sintering (SPS)”, *J. Solid State Chem.*, vol. 182, p. 396, 2009.

16. A. Lawley, “Atomization of specialty alloy powders”, *JOM*, vol. 33, p. 13, 1981.

17. Z.G. Lu, G.G. Xia, J.D. Templeton, X.H. Li, Z.M. Nie, Z.G. Yang, and J.W. Stevenson, “Development of $Ni_{1-x}Co_xO$ as the cathode/interconnect contact for solid oxide fuel cells”, *Electrochem. Comm.*, vol. 13, no. 6, p. 642, 2011.

18. W.-J. Shong, C.-K. Liu, W.-H. Shiu, and R.-Y. Lee, “Characteristics of Mn-Co and Ni-Co metal powders mixed with oxides as cathode contact materials for SOFC”, *Int. J. Hydrog. Energy,* vol. 44, no. 8, p. 4317, 2019.

19. X. Xin, L. Liu, Y. Liu, and Q. Zhu, “Novel perovskite-spinel composite conductive ceramics for SOFC cathode contact layer”, *Int. J. Hydrog. Energy,* vol. 43, no. 51, p. 23036, 2018.

20. Y.T. Yu, J.H. Zhu, and B.L. Bates, “Effect of precursor materials on the performance of the NiFe2O4-based spinel layer for SOFC cathode-side contact application”, *Solid State Ion.*, vol. 324, p. 40, 2018.

21. W. Wei, W. Chen, and D. G. Ivey, “Oxidation resistance and electrical properties of anodically electrodeposited Mn-Co oxide coatings for solid oxide fuel cell interconnect applications”, *J. Power Sources*, vol. 186, no. 2, p. 428, 2009.

22. E. Konysheva, J. Laatsch, E. Wessel, F. Tietz, N. Christiansen, L. Singheiser, and K. Hilpert, “Influence of different perovskite interlayers on the electrical conductivity between $La_{0.65}Sr_{0.3}MnO_3$ and Fe/Cr-based steels”, *Solid State Ion.*, vol. 177, no. 9-10, p. 923, 2006.

23. Z.G. Yang, G.G. Xia, J.W. Stevenson, and P. Singh, “Electrical contacts between cathodes and metallic interconnects in solid oxide fuel cells”, *J. Power Sources*, vol. 155, no. 2, p. 246, 2006.

24. X. Montero, F. Tietz, D. Stöver, M. Cassir, and I. Villarreal, “Comparative study of perovskites as cathode contact materials between an $La_{0.8}Sr_{0.2}FeO_3$ cathode and a Crofer22APU interconnect in solid oxide fuel cells”, *J. Power Sources*, vol. 188, no. 1, p. 148, 2009.

25. M.C. Tucker, L. Cheng, and L.C. DeJonghe, “Selection of cathode contact materials for solid oxide fuel cells”, *J. Power Sources*, vol. 196, no. 20, p. 8313, 2011.

26. Z.G.Yang, G.G. Xia, X.H. Li, and J.W. Stevenson, “$(Mn,Co)_3O_4$ spinel coatings on ferritic stainless steels for SOFC interconnect applications”, *Int. J. Hydrog. Energy,* vol. 32, no. 16, p. 3648, 2007.

27. W. Qu, L. Jian, D.G. Ivey, and J.M. Hill, “Yttrium, cobalt and yttrium/cobalt oxide coatings on ferritic stainless steels for SOFC interconnects”, *J. Power Sources*, vol. 157, p. 335, 2006.

28. Z. Yang, G. Xia, Z. Nie, J. Templeton, and J. W. Stevenson, “Ce-modified $(Mn,Co)_3O_4$ spinel coatings on ferritic stainless steels for SOFC interconnect applications”, *Electrochem. Solid-State Lett.*, vol. 11, no. 8, p. B140, 2008.

29. P.Y. Hou and J. Stringer, “The effect of reactive element additions on the selective oxidation, growth and adhesion of chromia scales”, *Mater. Sci. Eng. A*, vol. 202, p. 1, 1995.

30. J.W. Stevenson, Z.G. Yang, G.G. Xia, Z. Nie, and J.D. Templeton, “Long-term oxidation behavior of spinel-coated ferritic stainless steel for solid oxide fuel cell interconnect applications”, *J. Power Sources*, vol. 231, p. 256, 2013.
31. J.H. Zhu, M.J. Lewis, S.W. Du, and Y.T. Li, “CeO_2-doped $(Co,Mn)_3O_4$ coatings for protecting solid oxide fuel cell interconnect alloys”, *Thin Solid Films*, vol. 596, p. 179, 2015.
32. D. Udomsilp, D. Roehrens, N.H. Menzler, and R. Conradt, “Characterization of the contact resistance of cathodic SOFC contacting”, *ECS Trans.*, vol. 68, p. 751, 2015.
33. D. Kennouche, Q. Fang, L. Blum, and D. Stolten, “Analysis of the cathode electrical contact in SOFC stacks”, *J. Electrochem. Soc.*, vol. *165*, p. F677, 2018.
34. M.R. Weimar, L.A. Chick, D.W. Gotthold, and G.A. Whyatt, “Cost Study for Manufacturing of Solid Oxide Fuel Cell Power Systems”, *PNNL-22732*, 2013.
35. W.J. Quadakkers, J. Piron-Abellan, V. Shemet, and L. Singheiser, “Metallic interconnectors for solid oxide fuel assemblies – a review”, *Mater. High Temp.*, vol. 20, p.115, 2003.
36. S.L. Swartz, L.B. Thrun, R.K. Kimbrell, and K.M. Chenault, “Manufacturing cost analysis for YSZ-based flexcells at pilot and full scale production scales”, *Topical Report for DOE # DE-NT0004113*, May 9, 2011.